Journal of The Electrochemical Society, **161** (10) C501-C508 (2014)
0013-4651/2014/161(10)/C501/8/$31.00 © The Electrochemical Society

Microstructural Effects on Corrosion of AM50 Magnesium Alloys

R. Matthew Asmussen, W. Jeffrey Binns, Pellumb Jakupi, and David Shoesmith*,z

Department of Chemistry and Surface Science Western, Western University, London, Ontario, Canada

The influence of microstructure and aluminum distribution on the corrosion of three different casts of the magnesium AM50 alloy (sand, graphite, die) was studied in 1.6 wt% NaCl solution. The microstructure of the alloys and the distribution of individual elements were characterized using scanning electron microscopy (SEM) and energy dispersive X-ray analyzes. Differences in the morphology and distribution of corrosion damage were determined using SEM and confocal scanning laser microscopy. Weight change measurements and electrochemical impedance spectroscopy showed that the corrosion resistance improved in the order sand cast < graphite cast ≪ die cast. This increased resistance was shown to be attributable to the increasing tightness of the α-Mg/β-phase/Al-containing eutectic microstructural network, which led to an improved protection of the surface by Al-enriched eutectic and a decrease in the probability of initiating a major damage site on an α-Mg region with low Al content.
© 2014 The Electrochemical Society. [DOI: 10.1149/2.0781410jes] All rights reserved.

Manuscript submitted May 13, 2014; revised manuscript received July 14, 2014. Published July 26, 2014.

Mg alloys are attractive materials for automotive applications due to their high strength-to-weight ratio. However, one major deficiency is their inadequate corrosion resistance when exposed to aqueous and humid environments such as those experienced in automotive applications.[1–5] As the most electrochemically active structural material, Mg and its alloys are susceptible to galvanic corrosion when in electrical contact with a second metal/alloy,[6–8] as well as microgalvanic corrosion between the secondary microstructures and the α-Mg phases, both of which can rapidly accelerate corrosion.[9]

Al is commonly employed to improve the corrosion resistance of Mg alloys either as a direct coating [10] or through alloying,[11–13] and the corrosion resistance of Mg-Al alloys is commonly expressed in terms of their general Al content.[14,15] However, the alloying elements in Mg are generally segregated into distinct regions making their distribution throughout the microstructure a critical feature in determining corrosion resistance. Consequently, the effects on corrosion of many microstructural features have been studied. These features include grainsize[16] β-phase distribution,[17,18] β-phase morphology [17] and the interactions between the secondary microstructures.[19] In this study, the influence of the surface and sub-surface chemistry associated with the microstructural features on different castings of the AM50 alloy have been studied.

The commercial AM50 alloy, used for its exceptional castability,[20,21] contains a Mg-based α-phase, a β-phase ($Mg_{17}Al_{12}$) surrounded by Al-enriched eutectic α-phase, and Al-Mn intermetallics. Micro-galvanic couples between the β-phase and/or intermetallics and the α-phase matrix can accelerate the corrosion of the latter in aqueous and atmospheric environments.[22] In a previous study we investigated the microscale corrosion processes occurring on a sand-cast AM50 surface in chloride solution through repeated microscopic analyzes of corroded areas. From this work it was reported that; (1) increasing the Al content of a grain reduced its corrosion rate; (2) an Al-enrichment developed at the alloy surface in the eutectic regions of the material during the corrosion process providing protection; and (3) the distribution of Al was important in controlling the corrosion process as regions deficient in Al were susceptible to major corrosion damage. The aim of this study is to utilize the microscale approach developed [23] to quantify the extent and distribution of corrosion damage as an effect of microstructure size and distribution using sand-, graphite- and die-cast AM50 alloys. Two of the castings selected (sand-cast and graphite-cast) solidify close to equilibrium and generate larger microstructural features compared with die casting. By comparing three castings of the same alloy, any differences in elemental composition are minimalized, the main variable becoming the microstructure resulting from the casting procedure, in particular the size and distribution of the secondary phases and the Al content.

Experimental

Sample preparation.— AM50 alloys were supplied by General Motors (Canada). The as-received AM50 sand- and graphite-cast rods were machined into 1 × 1 × 0.7 cm electrodes. For the die-cast alloy square electrodes (1 × 1 × 0.2 cm) were machined from a 0.2 cm thick plate. The compositions of the alloys, determined using ICP-AES, comply with ASTM standard B275 and are listed in Table I. One side of the sample (1 cm^2) was tapped to connect to a threaded rod to allow electrical connection to external circuitry. The 1 cm^2 side of the sample to be examined was pre-treated as previously reported.[23] The samples were ground successively up to 4000 grit SiC. The ground alloy surface was then polished on a Struers DP-Dur cloth saturated in 3 μm Struers DP-Suspension A for 5 to 10 min with an ethanol/propanol mixture used in place of water as a lubricant. The final stage consisted of polishing, for 2–3 min, on a Struers OP-Chem cloth using an equal volume mixture of Struers OP-S Suspension and ethylene glycol, as an abrasive. The polished sample was rinsed and sonicated in anhydrous ethanol for 2 min and air dried and stored in a desiccator. The grinding and polishing procedure, which penetrated to a depth of > 10 μm, removed the outer casting skin from the die-cast alloy. This avoids the possibility of contaminants from the die casting process. For all electrochemical measurements, Struers EpoFix epoxy was used to mount the electrodes, leaving only the polished 1 cm^2 alloy surface exposed to electrolyte. For immersion experiments to assess surface damage only, the samples were not mounted in epoxy to facilitate subsequent analytical procedures.

Instrumentation.— Electron micrographs were obtained in back-scattered and secondary electron modes using either a LEO 440, Hitachi 3400-N Variable Pressure Scanning Electron Microscope or LEO 1540 XB SEM/FIB. X-ray energy dispersive spectroscopy (XEDS) maps were obtained using Quartz One software.

Depth profiles on un-corroded and corroded surfaces were measured with confocal laser scanning microscopy (CLSM) by detecting the reflected light intensity from a Zeiss 510 confocal, HeNe 633 nm laser. The polished sample surface was placed downward, suspended by a stage, facing the inverted objective. Light intensities were normalized into a depth profile by considering the number of steps (slices) through the focal plane, in the z-direction, required to reach the deepest region on the sample surface. The differences in light intensities were then converted to a distance. Optical micrographs were collected using a Zeiss Lunar V12 microscope equipped with an Axio 1.1 camera.

Intermittent immersion experiments.— Prior to a corrosion experiment, the polished surface was analyzed by SEM/XEDS and CLSM. The co-ordinates of an area of interest (AOI) were recorded (relative to a surface edge) so that the same area (275 μm × 450 μm) could subsequently be located after each of a series of immersions. Immersions were performed in a naturally aerated 1.6 wt% NaCl (reagent

*Electrochemical Society Fellow.
zE-mail: dwshoesm@uwo.ca

Downloaded on 2014-09-10 to IP 129.100.60.73 address. Redistribution subject to ECS terms of use (see ecsdl.org/site/terms_use) unless CC License in place (see abstract).

Table I. Compositions of the AM50 alloys determined with ICP-MS.

	Elements (wt%)			
	Al (range)	Mn	Zn	Mg
ASTM Standard	4.5–5.3	0.28–0.5	max 0.02	-
Sand Cast	4.85 ± (0.7)	0.29	0.06	94.78
Graphite Cast	4.50 ± (0.1)	0.34	0.06	95.04
Die Cast	4.81 ± (0.5)	0.30	0.03	94.70

grade, 99% assay) solution at 22 ± 2 °C. The polished face of the electrode was immersed suspended from a stainless steel rod with the electrolyte level located ∼ 1 to 2 mm above the polished surface.

After immersion, the corroded surface was rinsed with Nanopure water (18 MΩ-cm) and dried in an Ar stream. Sonication in anhydrous ethanol following each immersion was not performed as previously described[23] since this process was inconsequential in improving the analysis and any residual chloride on the surface could be removed solely with a water rinse. The corroded AOI was then analyzed using SEM/XEDS and CLSM, and compared to the same location prior to corrosion. This procedure was repeated after each of a series of immersions to determine the evolution of the corrosion damage morphology and the penetration depth with time. Following the final immersion weight loss measurements were performed. The accumulated corrosion product was then removed using a treatment with hexavalent chromium, which involved 60 s of gentle agitation in a 100 mL solution of 20 g CrO_3. After the treatment, the samples were sonicated in methanol for 10 s to remove any residual chromium solution from the surface, dried in an Ar stream, weighed and then placed immediately in a vacuum desiccator for 24 h to ensure complete dehydration prior to a final weighing. The rates measured from weight loss were corrected for total exposed surface area of the sample and the duration of exposure.

To investigate the distribution of corrosion on a wider area of the surface, experiments were performed on a 4 mm × 4 mm alloy sample mounted in Struers EpoFix epoxy so that only a single surface was exposed. The surface was polished as described previously.[23] The epoxy of the mounted sample and a corner of the sample were coated in carbon paint when necessary to improve conductivity of the sample surface for imaging. The paint was removed with ethanol prior to the initial immersion. The entire 4 × 4 mm polished surface was imaged at 150 x for the sand- and graphite-cast samples and 500 x for the die-cast using a Hitachi SU6600 Field Emission SEM. The images were then stitched using Image-Pro Plus 7.0 into a final surface montage image of the entire 4 mm × 4 mm surface. The sample was then immersed in chloride solution and corrosion analyzes performed after a series of immersions. Between each immersion the surface was reanalyzed by SEM and a series of montage images constructed.

Electrochemical analysis.— All electrochemical measurements were performed in a standard three-electrode cell with a saturated calomel reference electrode (SCE) and a 4 cm^2 Pt foil counter electrode. Solutions were prepared using NaCl (reagent grade 99% assay) and NanoPure water (18.2 MΩ · cm). All experiments were performed at 22 °C ± 2 °C. After each measurement the electrolyte was discarded and the cell rinsed with NanoPure water.

Electrochemical responses were measured with a 1287 Solartron potentiostat coupled to a 1260 Solartron frequency response analyzer for electrochemical impedance spectroscopy (EIS) measurements. Prior to each potentiodynamic polarization (PDP) scan, the corrosion potential (E_{CORR}) was allowed to stabilize for 20 min. Then, a PDP scan was started 200 mV below E_{CORR} and the potential scanned in the positive direction until either the potential reached 200 mV above E_{CORR}, or, to avoid severe damage to the alloy surface, the measured current density reached 1 mA/cm^2.

EIS measurements were performed after 10 h of immersion at E_{CORR}. A sinusoidal potential perturbation of ± 10 mV was applied around E_{CORR}, and the current response recorded over the frequency range, 10^5 Hz to 10^{-3} Hz. Eleven data points per frequency decade were recorded. Subsequently, a one point per decade reverse scan was recorded from 10^{-2}–10^5 Hz to ensure steady-state was maintained throughout the EIS measurement. Kramers – Kronig transforms were applied to confirm the validity of the data, and non-valid data points were removed from the presented spectra.[24]

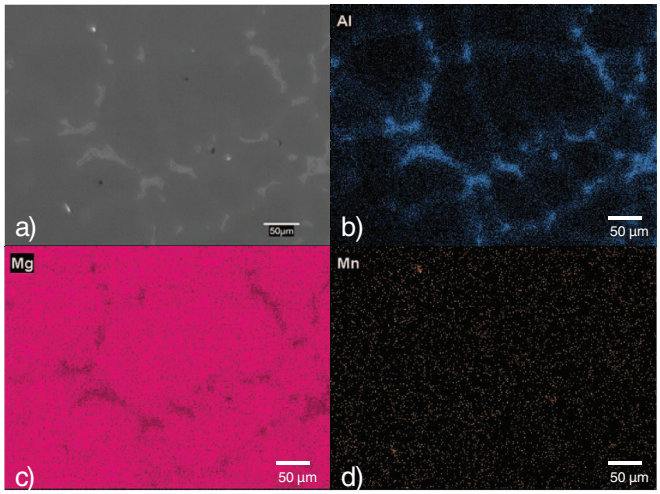

Figure 1. a) SEM image of a polished sand cast AM50 sample and the corresponding EDX maps showing the distribution of b) Al, c) Mg and d) Mn.

Results

Alloy characterization.— Figures 1 to 3 show SEM micrographs of selected areas of interest (AOI) on the sand-cast (Figure 1), graphite-cast (Figure 2) and die-cast (Figure 3) alloys. The backscatter SEM images are shown in (a) and the corresponding XEDS maps in (b) Al, (c) Mg and (d) Mn. The differences in microstructure can best be appreciated by comparing the sizes of the β-phase structures, (seen as the light gray regions in the SEM images which correspond to higher Al signals in the XEDS maps). Measured along the longest axis of the β-phase, the sand-cast ranges from > 100 µm to 10 µm, the graphite-cast from 50 µm to 5 µm and the die-cast is < 10 µm. Smaller β-phase sizes produce a more tightly linked network of

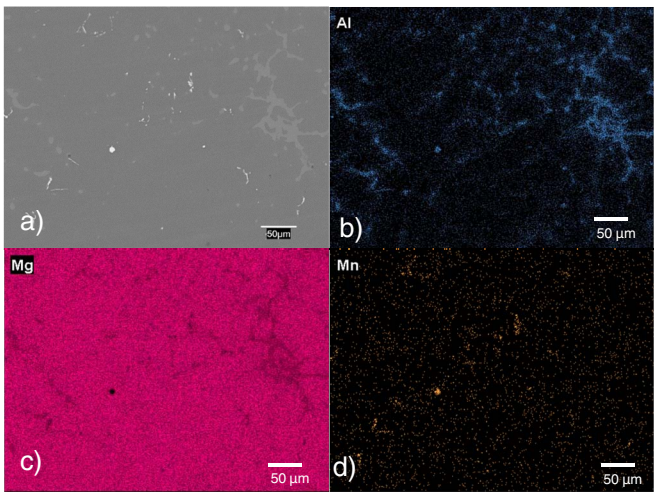

Figure 2. a) SEM image of a polished graphite cast AM50 alloy and the corresponding EDX maps showing the elemental distribution of b) Al, c) Mg and d) Mn.

Downloaded on 2014-09-10 to IP 129.100.60.73 address. Redistribution subject to ECS terms of use (see ecsdl.org/site/terms_use) unless CC License in place (see abstract).

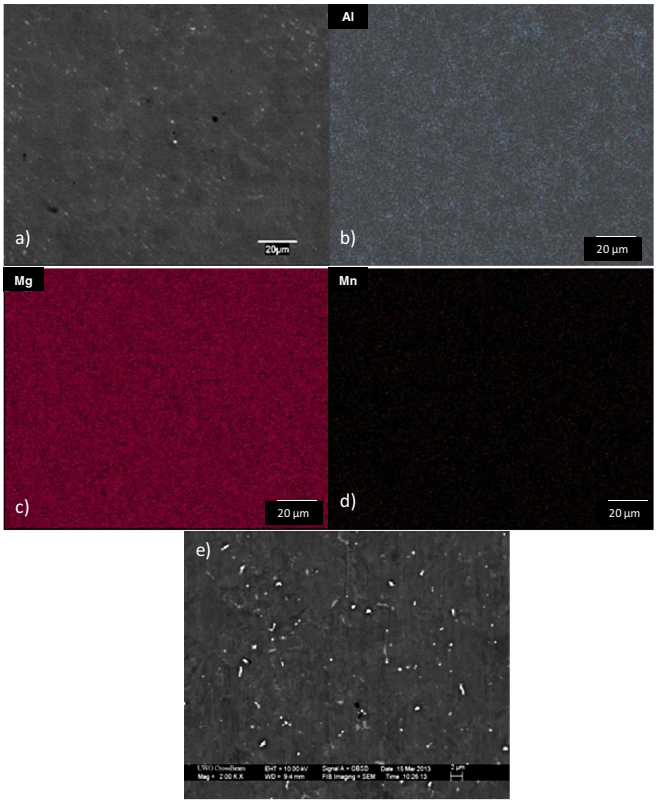

Figure 3. a) SEM image of a polished die cast AM50 sample and the corresponding EDX maps showing the distribution of b) Al, c) Mg and d) Mn; E) a magnified SEM image showing the distribution of β-phase (light gray areas) and intermetallics (white areas).

Al-rich eutectic α-phase connecting the β-phase, achieving a more even distribution of Al throughout the alloy. This network and its coverage can be seen in the Al maps of Figures 1b, 2b, and 3b. The distinct signal from AlMn intermetallics (bright white spots in the SEM images) can also be observed in the Mn maps of Figure 1b, 2d. On the die-cast alloy, the AlMn intermetallics are much smaller ($<1\mu m$) and are not resolved at the magnification of the XEDS map in Figure 3d. Their presence is confirmed in the SEM image in Figure 3e which shows the die-cast surface at a higher magnification.

Electrochemical behavior.— E_{CORR} measurements over a 24 h immersion period, Figure 4, showed the average E_{CORR} values to be −1.59 V, −1.56 V, and −1.54 V for the sand-, graphite- and die-cast alloys, respectively.

PDP measurements are presented in Figure 5. The casts displayed nearly identical behavior in the cathodic region, −1.80 V to −1.55 V, suggesting the kinetics of water reduction were similar on all three alloys. At potentials positive to E_{CORR}, the die- and graphite-cast alloys appeared to be forming a protective (at least partially) oxide layer as the current became increasingly less potential-dependent as the potential was increased, over the range −1.50 V and – 1.44 V. However, the sudden current increase (for $E > -1.475$ V) indicated the breakdown of any film formed and the onset of rapid dissolution. The die-cast alloy commonly exhibited slightly higher breakdown potentials than the graphite-cast alloy, although the difference is small (<10 mV) as indicated by the colored bars on both plots. For the sand-cast alloy no early attempt to form a corrosion-resistant oxide was observed with the current immediately, and reproducibly, rising to high values as the applied potential became positive to E_{CORR}.

Differences between the casts were also apparent in the EIS spectra, Figure 6. The Nyquist plots for the sand-cast (green) and graphite-cast (blue) alloys display a single capacitive and one inductive feature, with the impedance at the low frequency limit higher for the graphite-cast than the sand-cast alloy, indicating a lower corrosion rate. The Nyquist plot for the die-cast alloy (red), exhibits similar features, but also contains a second capacitive loop and the low frequency impedance is considerably larger than for the other two alloys.

While the EIS behavior, recorded after 10 h of exposure, and the PDP measurements, recorded after cathodic polarization, are not directly comparable, the trends in behavior between the three castings is consistent for the two measurements. According to the PDP scan the ability to resist the establishment of general active conditions, as indicated by the major current increases at positive potentials, is in the order, die > graphite ≫ sand. This is in the same order as the

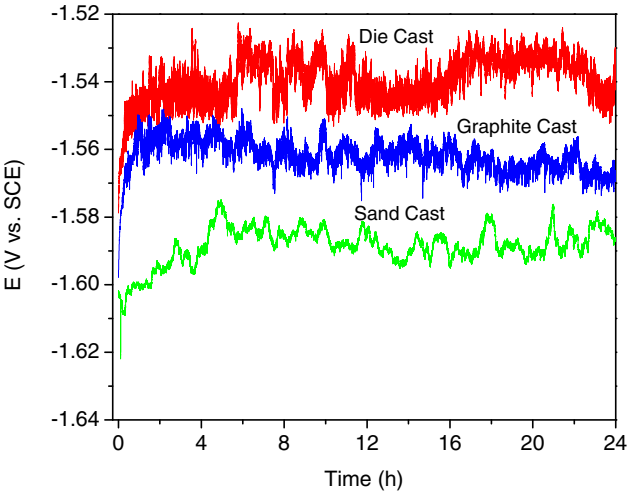

Figure 4. Progression of E_{CORR} of the polished sand cast (green), graphite cast (blue) and die cast (red) AM50 alloys recorded in 1.6 wt% NaCl.

Downloaded on 2014-09-10 to IP 129.100.60.73 address. Redistribution subject to ECS terms of use (see ecsdl.org/site/terms_use) unless CC License in place (see abstract).

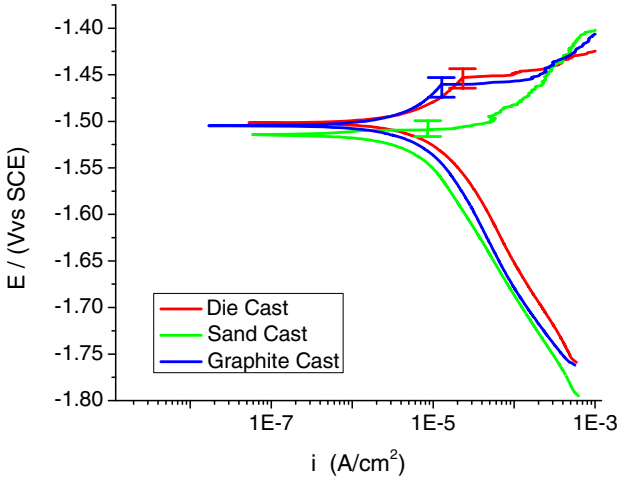

Figure 5. polarization (PDP) curves for the sand cast (green), graphite cast (blue) and die cast (red) AM50 alloys recorded in 1.6 wt% NaCl at a scan rate of 0.5 mV/s after 20 min at E_{CORR}. The colored bars display the ranges of breakdown potentials measured in repeated scans.

polarization resistances (the real resistance as the low frequency limit is approached) observed in the EIS measurements.

Corrosion behavior in 1.6 wt% NaCl.— Information on the nature and distribution of corrosion damage was obtained using a combination of SEM and CLSM on corroded samples. Following SEM and CLSM imaging of a selected AOI on a freshly polished sample, the samples were immersed in 1.6 wt% NaCl for a sequence of 24 h exposure periods. After each immersion, the AOI was re-located and imaged again by SEM and CLSM to monitor alterations to the corroded surface. The images recorded after each 24 h immersion are presented in Figure 7 for the sand- cast, Figure 8 for the graphite-cast, and Figure 9 for the die-cast alloys. The larger α-Mg grains in the sand-cast alloy were preferentially corroded, Figure 7, and appear as dark regions in the SEM images and depressions in the CLSM images. As corrosion progressed, a skeletal network rich in Al [25] was left behind and some domes of corrosion product appeared, marked with a red arrow in Figure 7. The green arrows identify the same α-grain in the SEM and CLSM images after 24 h, with this grain in the same location after the subsequent immersions. A detailed description of the corrosion behavior of this alloy has been published.[23]

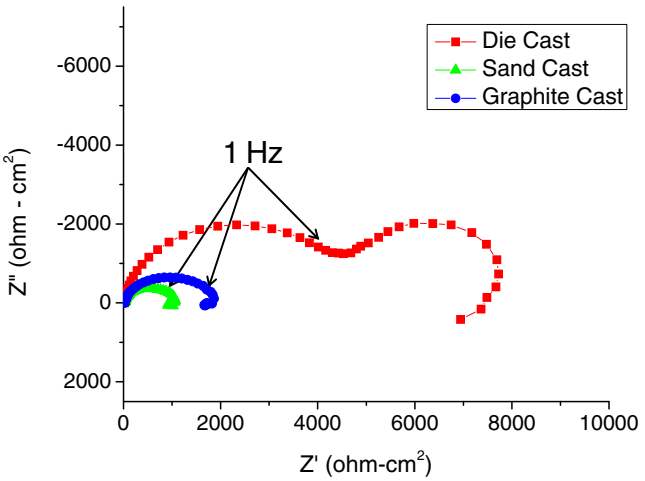

Figure 6. Nyquist plots for the sand cast (green), graphite cast (blue) and die cast (red) alloys recorded in 1.6 wt% NaCl after 10 h of exposure.

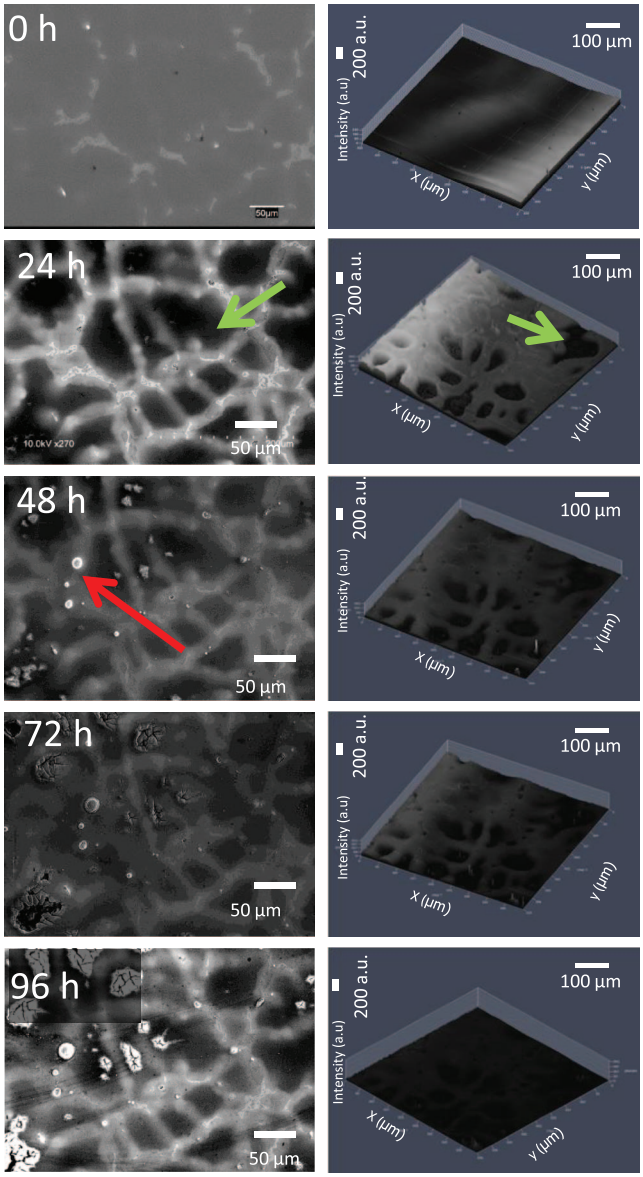

Figure 7. SEM micrographs and CLSM images of the sand cast AM50 alloy after a sequence of 24 h intermittent immersions in 1.6 wt% NaCl. The green arrow indicates the same α-Mg grain in the SEM and CLSM image The red arrow identifies domes of corrosion product appearing over sites of higher cathodic activity.

The graphite-cast AM50 alloy, Figure 8, developed a similar corrosion morphology through an identical series of immersions, but corroded α-phase regions were considerably smaller in dimension, compared with the sand-cast alloy shown in Figure 7. On the die-cast alloy, Figure 9, the corroded α-Mg regions were very small compared to those on the other two casts and the remaining uncorroded β-phases formed a much more extensive network leading to a substantial reduction in the overall extent of corrosion damage to the surface. In the SEM images recorded after 24 and 48 h of immersion, Figure 9, the dark rectangles were an artifact of carbon stitching during XEDS mapping of the polished surface.[26] No influence of this procedure on the corrosion behavior was observed. After 72 h of immersion, the dark region in the bottom of the CLSM image indicates the accumulation of white corrosion product detected in the corresponding SEM image. This mass of corrosion product did not coherently reflect the laser beam and no return signal was detected in the CLSM image.

Downloaded on 2014-09-10 to IP 129.100.60.73 address. Redistribution subject to ECS terms of use (see ecsdl.org/site/terms_use) unless CC License in place (see abstract).

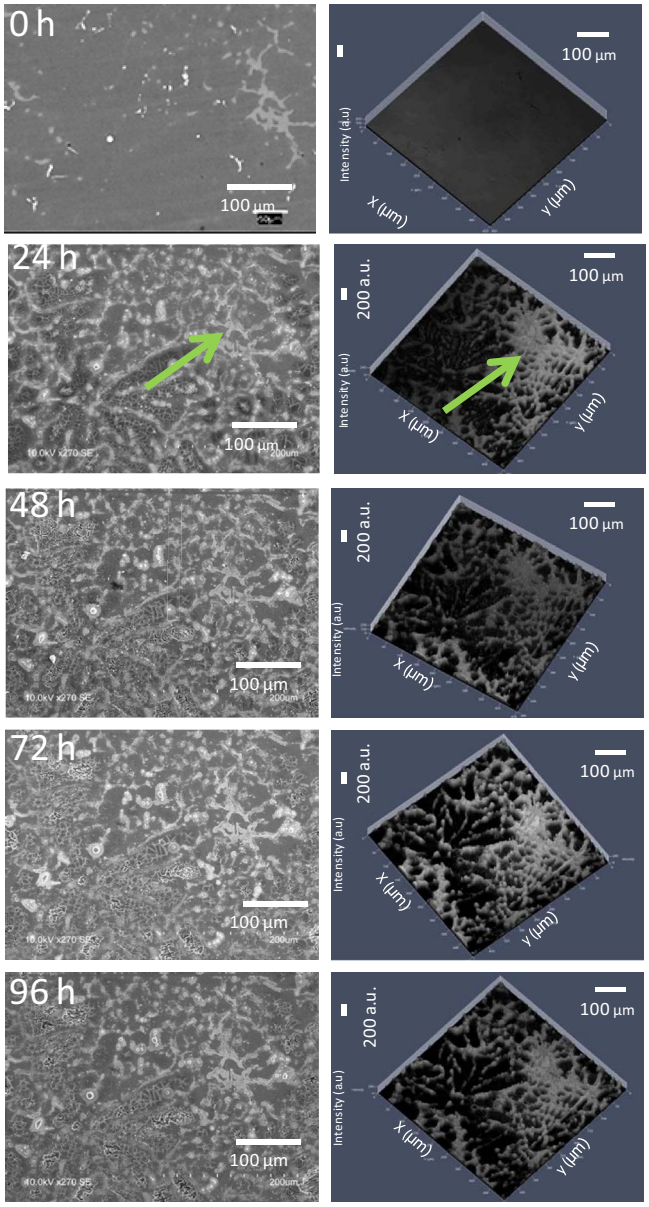

Figure 8. SEM micrographs and CLSM images of the graphite-cast AM50 alloy after a sequence of 24 h intermittent immersions in 1.6 wt% NaCl. The green arrows relate the same features in the SEM and CLSM images.

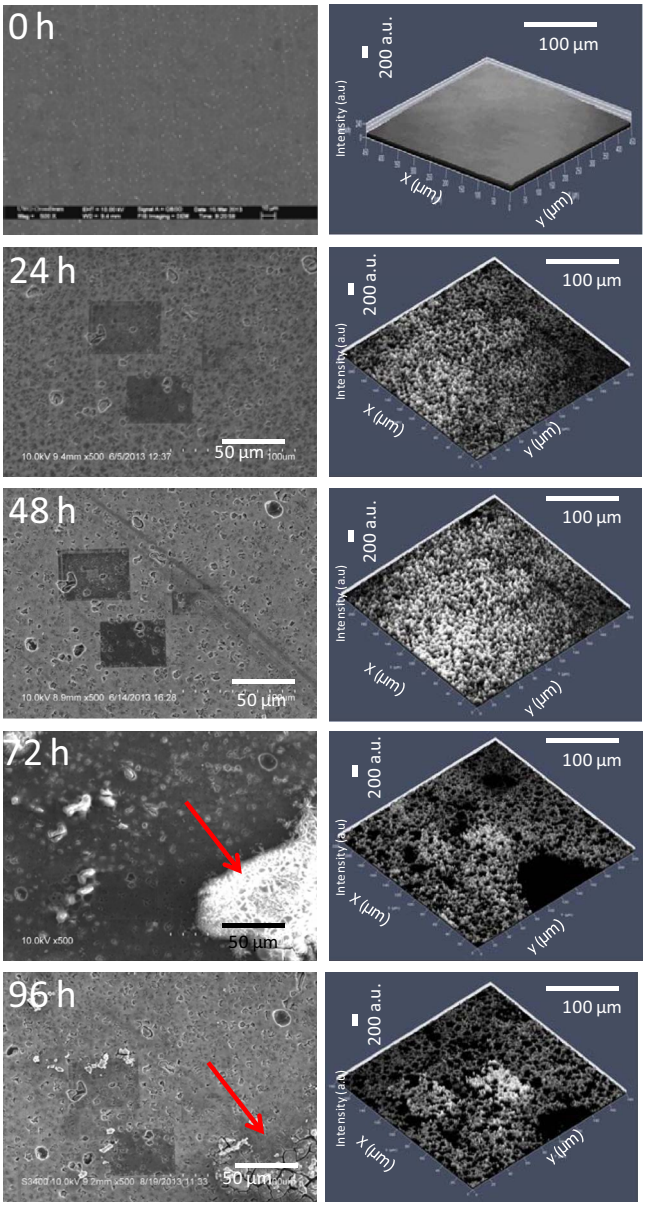

Figure 9. SEM micrographs and CLSM images of the die-cast AM50 alloy after a sequence of 24 h intermittent immersions in 1.6 wt% NaCl. The green arrow identify the same feature in the SEM and CLSM images. The red arrow shows the location of a corrosion product deposit in the SEM images.

After 96 h of immersion, this corrosion product fell off, Figure 9, confirming its general lack of adherence to the alloy surface.

Following the series of immersions in 1.6 wt% NaCl weight loss measurements were performed and the mean measured rates are presented in Table II. Based on these rates, the corrosion resistances are in the order sand-cast < grahite-cast ≪ die-cast, as observed for the sequence of polarization resistances determined qualitatively from the EIS spectra and consistent with the evidence from SEM/CLSM images that the more widespread distribution of Al limits the extent of corrosion.

The occurrence of large areas of corrosion, observed here on the die-cast alloy after 72 h, were also observed previously during the corrosion of the AM50 sand-cast alloy.[23] While the general distribution of corrosion damage involving microgalvanic coupling could be successfully followed as illustrated in Figures 7, 8 and 9, the capture of a major corrosion event in the small area imaged by CLSM was not guaranteed. Examinations of larger surface areas and the successful identification of major corrosion events were achieved by montage imaging of 4 mm x 4 mm samples of the three alloys. Using this approach, we showed previously that the sand-cast alloy was susceptible to such major corrosion events after < 2 h of exposure in 1.6 wt% NaCl.[23] These events were shown to initiate in regions of α-Mg grains depleted in Al content.

Surface montage images of the graphite-cast AM50 alloy before, and following, short periods of corrosion are displayed in Figure 10.

Table II. Corrosion rate, in mg/cm^2/d, of the sand, graphite and die cast alloys from weight loss measurements in 1.6 wt% NaCl with the standard deviation (SD).

	Weight Loss mg/cm^2/d	SD
Sand Cast	0.93	0.10
Graphite Cast	0.70	.073
Die Cast	0.22	0.11

Downloaded on 2014-09-10 to IP 129.100.60.73 address. Redistribution subject to ECS terms of use (see ecsdl.org/site/terms_use) unless CC License in place (see abstract).

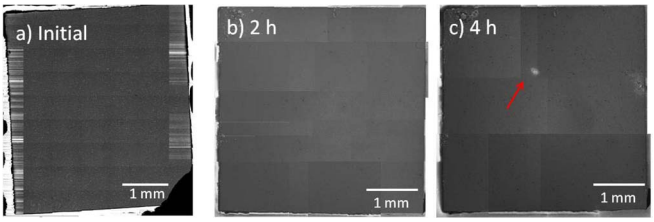

Figure 10. SEM montage micrographs of the graphite cast AM50 after a) polishing, b) 2 h and c) 4 h of immersion in 1.6 wt% NaCl. The red arrow in c) shows the first major corrosion event to initiate.

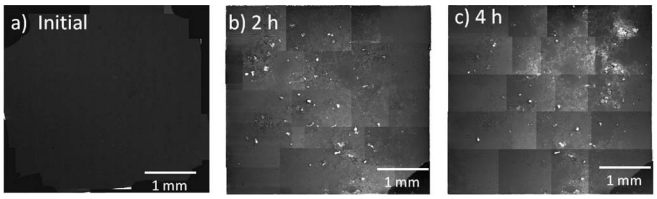

Figure 11. SEM montage micrographs of die cast AM50 after a) polishing, b) 2 h and c) 4 h of immersion in 1.6 wt% NaCl.

Figure 10a shows the electron backscatter SEM montage map of the polished alloy prior to a sequence of 1 h intermittent immersions in 1.6 wt% NaCl. Following 2 h of immersion, Figure 10b, no major corrosion damage sites had initiated. The damage observed in the top left region of the montage occurred in an occluded location at the interface formed between the epoxy and the alloy edge[27] and was not representative of the planar surface behavior. After 4 h of immersion a single major event had initiated, and is indicated in the image with a red arrow, Figure 10c.

The montage image for the freshly polished die-cast alloy is shown in Figure 11a. Following two 1 h periods of corrosion in 1.6 wt% NaCl, Figure 11b, the damage was more obvious but possessed a different morphology to that observed on the graphite-cast alloy. Conductive carbon paint had to be reapplied to a corner (bottom right) of the sample following the initial immersion to overcome charging of the corrosion product while montage imaging the damaged surface. While no major individual events were observed, corrosion damage spread laterally across the surface of the alloy. After 4 h of immersion, a major event initiated and is seen in the top right of Figure 11c.

The differences in corrosion damage morphologies observed on the three cast alloys are summarized in the stereomicrographs of the general alloy surfaces recorded following 96 h of immersion, Figure 12. When a larger area of the alloy surface is visible, the sand-cast, Figure 12a, and graphite-cast, Figure 12b, alloys show areas of extensive corrosion damage, which are much larger on the sand cast than the graphite cast. By contrast, corrosion damage propagated laterally along the surface of the die-cast alloy, Figure 12c, and deeply penetrating events were less frequently initiated. This lateral propagation of damage has been observed previously on Mg and Mg alloys.[28–31] This change in damage morphology between the general deep penetration of α-Mg grains and the propagation of shallow lateral damage is reflected in the EIS responses and the corrosion rates (Table II).

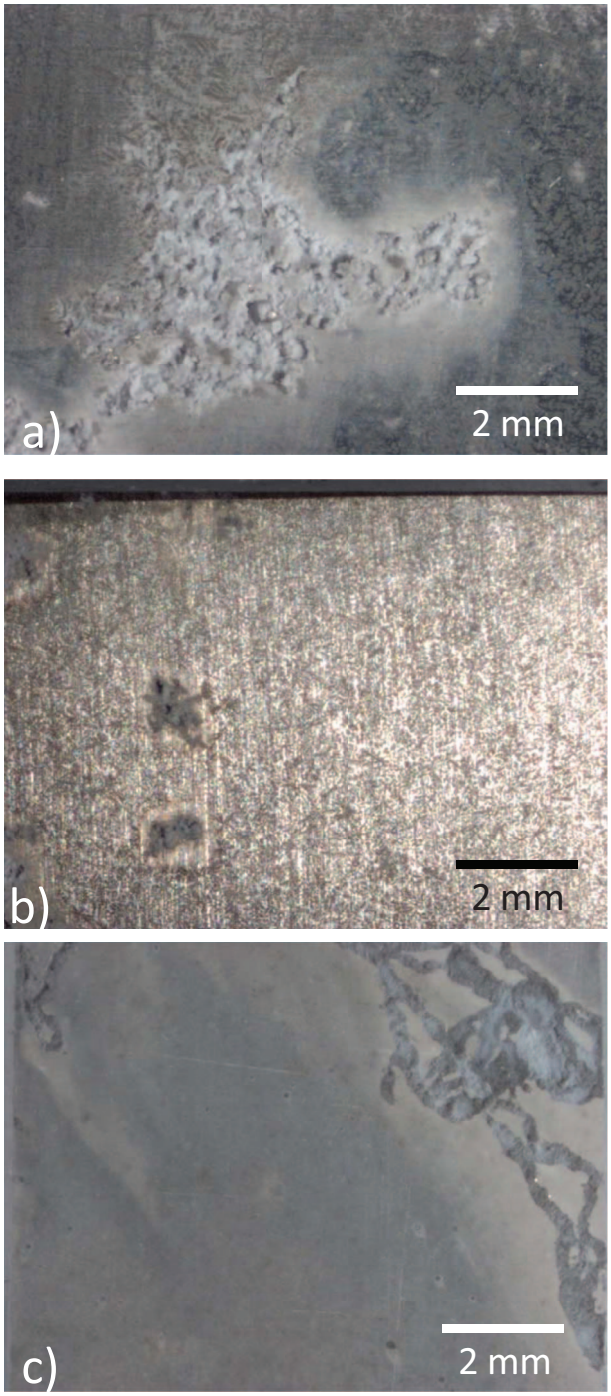

Figure 12. Stereo micrographs of the a) sand, b) graphite and c) die cast AM50 alloys following a 96 h immersion in 1.6 wt% NaCl. The white blotches on the sand and graphite cast alloys indicate the accumulation of corrosion product in the α-Mg regions. The dark lines in c) show corrosion damage propagates laterally across the surface on the die cast alloy.

Discussion

The selection of three casts of the same Mg alloy minimizes the influence of composition and allows the influence of microstructure and the distribution of alloying elements to be investigated. The difference in electrochemical response between the three casts is evident in the E_{CORR}, PDP and EIS measurements. The PDP scans demonstrate that the kinetics of the H_2O reduction reaction did not change significantly with alloy cast. This indicates that, in general, the differences in corrosion response between the three casts were predominantly due to the differences in anodic behavior. In the PDP measurements, following the cathodic polarization sweep, the graphite- and die-cast alloys displayed similar behavior. No attempt was made to extract quantitative corrosion rates since the Tafel extrapolation approach is unreliable for Mg materials.[27]

A difference in the mode of corrosion between the three casts is evident in the EIS measurements and micrographs of the alloy surfaces, which show the die-cast had a significantly higher low frequency impedance than the other two casts indicating a lower general corrosion rate.[32] By contrast, the impedance at the low frequency limit

Downloaded on 2014-09-10 to IP 129.100.60.73 address. Redistribution subject to ECS terms of use (see ecsdl.org/site/terms_use) unless CC License in place (see abstract).

is only slightly larger for the graphite- than the sand-cast alloy. The sand- and graphite-cast alloys exhibit only one capacitative and an inductive response, whereas the die-cast alloy yields two capacitative responses in addition to the inductive feature. The presence of two capacitive responses in the Nyquist plot of Mg alloys is common, and the transition from one to two responses was reported for the corrosion of the Mg alloy AZ91 in Na_2SO_4 and attributed to the thickening of the corrosion product layer.[32] Contradictory explanations have been proposed to explain the origin of these two responses. The high frequency response has been attributed to the charge transfer process, $Mg \rightarrow Mg^{2+}$, at the alloy surface, and the medium frequency response to the diffusion of Mg^{2+} through the thickening porous $Mg(OH)_2$ corrosion product film.[32] However, it has also been reported that the high frequency loop can be attributed to the behavior of the surface films and the mid frequency response to the charge transfer process.[33] On Mg materials a response involving two capacitative responses coupled to an inductive response has also been attributed to localized or microgalvanic corrosion.[34] The inductive feature observed in the Nyquist plots is common to corroding Mg and Mg alloy systems and has been linked to the relaxation of surface adsorbed intermediates in the anodic reaction,[35] to the dissolution of a partially protective film,[36] or most recently with accelerated anodic dissolution.[37] The species responsible for the inductive response are yet to be determined.[37] The presence of the inductive feature in the spectra in Figure 6 indicates that the input potential signal can still detect the surface processes on the substrate alloy irrespective of whether a surface corrosion product is present or not. The spectra clearly demonstrate an alteration in the mode of corrosion on the die-cast alloy compared to the sand- and graphite-cast alloys. The presence of the mid-frequency response suggests corrosion inhibition by a $Mg(OH)_2$ corrosion product film. That corrosion is suppressed on this cast is confirmed by the corrosion rates obtained from weight loss measurements. In fact, the ratio of the rates for the three casts (Table II) is very similar to the ratios of polarization resistances estimated from EIS spectra. This change in EIS behavior suggests the alloy microstructure and subsequent distribution of the alloying elements, especially Al, plays a primary role in the corrosion behavior. A more extensive EIS study is underway.

The shift in E_{CORR} to more negative values accompanied by the general decrease in interfacial impedance is consistent with the CLSM analysis which shows the corrosion susceptible area of the surface increases in the order die-cast $\ll$ graphite-cast $<$ sand-cast. During intermittent immersion experiments, the sand- and graphite- cast alloys exhibit corrosion of the α-Mg regions leaving behind an interlinked skeletal network of eutectic-α phase characterized by its high Al content. The CLSM micrographs in Figure 7a and 7b show the secondary β-phases and lightly corroded eutectic network are more tightly compact on the graphite-cast compared to the sand-cast alloy, which would allow a more extensive area of the alloy surface to generate a protective Al-enrichment on the surface during corrosion.[11,23,25] This increased area of protected surface would account for the slightly improved corrosion resistance. As demonstrated by the montage imaging, this decrease in regions of the surface depleted in Al also extends the time required to initiate extensive corrosion propagation sites. This slight improvement notwithstanding, both casts exhibit significant corrosion penetration into the surface via the α-Mg regions.

On the die-cast alloy this skeletal network is considerably tighter than on the other two casts, leading to a higher surface density of Al-containing eutectic, which appears to limit the depth of corrosion penetration on α-Mg regions leading to extensive lateral propagation of corrosion across the surface as opposed to penetration into the surface, as suggested previously.[38,39] Since this tight network of Al enriched eutectic is three-dimensional, additional subsurface areas are exposed as corrosion progresses further, hindering damage propagation into the alloy. Despite this, the possibility of initiation of a major damage site is not eliminated if there are areas where Al is more extensively depleted. The appearance of corrosion damage tracking along the alloy surface was also recently attributed to alloy heterogeneity and Al distribution on an AZ31 alloy,[30] a similar effect to that observed in this work with decreasing microstructure size.

Previous studies showed a similar influence of microstructural size, the corrosion resistance of a die-cast AZ91 Mg alloy with its outer "skin" ($<$10 μm in thickness) intact being higher than that of a slowly solidified AZ91 alloy. The improved corrosion resistance was attributed to the smaller α-grains and β-phase in the skin, arising from the rapid solidification of the outer surface in contact with the die, and a decreased porosity.[40] As noted in the experimental section the skin on our die-cast alloy was removed prior to characterization of the alloy and its corrosion exposure.

The reduction in the size of microstructural features (α-Mg grains, β-phase) leading to a more even distribution of Al on the AM50 alloy induces not only an alteration in electrochemical behavior and corrosion rate but also a change in corrosion damage morphology. This influence of microstructure is consistently observed in the E_{CORR} measurements (Figure 4), the interfacial impedance (Figure 6), general corrosion rates (Table II), and the area of the surface observed to be corrosion resistance in SEM/ CLSM imaging (Figures 7–9) and susceptibility to extensive corrosion damage (Figures 10–11).

Previous studies have also shown that die casting improved the corrosion performance over the ingot material for AZ91,[41] and that a finer grain size improved the corrosion of Mg alloys.[42–44] Our previous study on the sand-cast alloy showed that the Al content of individual α-phase regions directly affected the extent of corrosion damage, an influence that would be independent of grain size.[23] Along with a reduction in the α-Mg surface area, the average size of the secondary microstructural constituents also decreases, resulting in a more widespread distribution of Al present in the eutectic α-Mg regions around the β-phase network. This increases the potential area of the surface and even the subsurface capable of acting as a corrosion resistant barrier as corrosion progresses.

Conclusions

The corrosion rates of AM50 alloys, determined from weight loss measurements, and also qualitatively by EIS, increased in the order sand-cast $<$ graphite-cast $\ll$ die-cast. CLSM showed this improvement could be attributed to the increasingly compact nature of the secondary microstructure (β-phase + Al-containing eutectic) through this sequence.

As corrosion progressed, the higher Al content in the eutectic surrounding the β-phase protected these regions from extensive corrosion and reduced the likelihood that major corrosion sites would initiate in the core of α-Mg grains with low Al content.

Since this tight network of Al-enriched eutectic is three dimensional in the die-cast alloy, the exposure of additional subsurface areas of Al-enriched eutectic forced corrosion to propagate laterally rather than penetrate deeply into this cast.

Despite this improvement in corrosion resistance the initiation of major corrosion damage sites is not eliminated in the die-cast alloy.

Acknowledgments

This work was funded by a Collaborative Research and Development grant supported by NSERC and General Motors Canada. We acknowledge the staff at Surface Science Western, ZAPLab, and Integrated Microscopy at the Biotron Research Institute at Western University for their time and instrument use, Janine Mauzeroll and her group at McGill University and Gianluigi Botton and staff at the Canadian Center for Electron Microscopy at McMaster University for the continuing collaboration in this project. This paper is dedicated to the memory of J.W. Asmussen.

References

1. P. J Blanchard, D. J. Hil, G. T. Bretz, and R. C. McCune, *Essential Reading in Mag. Tech.* p. John Wiley & Sons, New York 463 (2005).
2. M. K. Kulecki, *Int. J Adv Manuf Tech*, **39**, 851 (2008).
3. G. Song, *Adv. Eng. Mat.*, **7**, 563 (2005).
4. G. Song, D. St. John, C. Bettles, and G. Dunlop, *JOM*, **57** 54 (2005).

Downloaded on 2014-09-10 to IP 129.100.60.73 address. Redistribution subject to ECS terms of use (see ecsdl.org/site/terms_use) unless CC License in place (see abstract).

5. R. McCune et al., *Mag. Tech.*, **2013** 163 (2013).
6. K. B. Desphande, *Corros. Sci.*, **62** 184 (2012).
7. L. Lacroix, C. Blanc, N. Pebere, B. Tribollet, and V. Vivier, *J. Electrochem. Soc.*, **156** C259 (2009).
8. K. B. Deshpande, *Corros. Sci.*, **52**, 2819 (2010).
9. G. Song and A. Atrens, *Adv. Eng. Mat.*, **5**, 837 (2003).
10. J. K. Chang, S. Y. Chen, W. T. Tsai, M. J. Deng, and I. W. Sun, *J. Electrochem. Soc.*, **155** C112 (2008).
11. J. H. Nordlien, K. Nisancioglu, S. Ono, and N. Masuko, *J. Electrochem. Soc.*, **144**, 461 (1997).
12. R. Lindstrom, J. E. Svensson, and L. G. Johansson, *J. Electrochem. Soc.*, **149**, B103 (2002).
13. P. Volovitch, M. Serdechnova, and K. Ogle, *Corrosion*, **68** 557 (2012).
14. M. Liu, P. Uggowitzer, A. Nagasekhar, P. Schmutz, M. Easton, G. Song, and A. Atrens, *Corros. Sci.*, **51**, 602 (2009).
15. Y. L. Cheng, T. W. Qin, H. M. Wang, and Z. Zhang, *Trans. Nonferrous Met. Soc. China*, **19**, 517 (2009).
16. K. D. Ralston and N. Birbilis, *Corrosion*, **66**, 1 (2010).
17. M. Zhao, M. Liu, G. Song, and A. Atrens "Influence of the β-phase morphology on the corrosion of the Mg alloy AZ91," *Corros. Sci.*, **50**, 1939 (2008).
18. T. Zhang, Y. Shao, G. Meng, Z. Cui, and F. Wang, *Corros. Sci.*, **53**, 1960 (2011).
19. F. Andreatta, I. Apachitei, A. A. Kondentsov, J. Dzwonczyk, and J. Duszczyk, *Electrochim. Acta*, **51**, 3551 (2006).
20. V. Y. Gertsman, L. Jian, S. Xu, J. P. Thomson, and M. Sahoo, *Metallurg. and Mat. Trans. A*, **36A**, 1989 (2005).
21. C. Blawert, D. Fechner, D. Hoche, V. Heitmann, W. Dietzel, K. U. Kainer, P. Zivanovic,C. Scharf, A. Ditze, J. Grobner, and R. Schmid-Fetzer, *Corros. Sci.*, **52**, 2452 (2010).
22. M. Jonsson, D. Persson, and R. Cubner, *J. Electrochem. Soc.*, **154**, C684 (2007).
23. R. M. Asmussen, P. Jakupi, M. Danaie, G. Botton, and D. W. Shoesmith, *Corros. Sci.*, **75**, 114 (2013).
24. B. Boukamp, *J. Electrochem. Soc.*, **142**, 1885 (1995).
25. M. Danaie, R. M. Asmussen, P. jakupi, D. Shoesmith, and G. Botton, *Corros. Sci.*, **77**, 151 (2013).
26. D. Lau, A. E. Hughes, T. M. Muster, T. J. Davis, and A. M. Glenn, *Microscopy and Microanal.*, **16**, 13 (2010).
27. A. Atrens, *ECS Trans.*, **50**, 335 (2013).
28. P. Schmutz, V. Guillaumin, R. S. Lillard, J. A. Lillard, and G. S. Frankel, *J. Electrochem. Soc.*, **150**, B99 (2003).
29. O. Lunder, J. E. Lein, S. M. Hesjevik, T. K. Aune, and K. Nisancioglu, *Werkst. Korros.*, **45**, 331 (1994).
30. W. Song, H. J. Martin, A. Hicks, D. Seely, C. A. Walton, W. B. Lawrimore II, P. T. Wang, and M. F. Horstemeyer, *Corros. Sci.*, **78**, 353, (2014).
31. G. Williams, H. ap. Llwyd, and R. Grace, *Electrochim. Acta*, **109**, 489 (2013).
32. G. Galicia, N. Pebere, B. Tribollet, and V. Vivier, *Corros. Sci.*, **51**, 1769 (2009).
33. W. Liu, F. Cao, A. Chen, L/ Chang, J. Zhang, and C. Cao, *Corrosion*, **68**, 045001–1 (2012).
34. F. Cao, Z. Shi, J. Hofstetter, P. Uggowitzer, G. Song, M. Liu, and A. Atrens, *Corros. Sci.*, **75**, 78 (2013).
35. G. Baril, C. Blanc, and N. Pebere, *J. Electrochem. Soc.*, **148**, B489 (2001).
36. W. Liu, F. Cao, A. Chen, L. Chang, J. Zhang, and C. Cao, *Corrosion*, **68**, 045001–1 (2012).
37. A. D. King, N. Birbilis, and J. Scully, *Electrochim. Acta*, **121**, 394, (2014).
38. G. Song and A. Atrens, *Adv. Eng. Mat.*, **1**, 11 (1999).
39. D. Sachdeva, *Corros. Sci.*, **60**, 18 (2012).
40. G. Song, A. Atrens, and M. Dargusch, *Corros. Sci.*, **41**, 249 (1999).
41. R. Ambat, N. N. Aung, and W. Zhou, *Corros. Sci*, **42**, 1433 (2000).
42. M. Alvarez-Lopez, M. D. Pereda, J. A. del Valle, M. Fernandez-Lorenzo, M. C. Garcia-Alonso, O. A. Ruano, and M. L. Escudero, *Acta Biomater.*, **6**, 1763 (2010).
43. G. R. Argade, S. K. Panigrahi, and R. S. Mishra, *Corros. Sci.*, 145 (2012).
44. N. N. Aung and W. Zhou, *Corros. Sci.*, **52**, 589 (2010).

Downloaded on 2014-09-10 to IP **129.100.60.73** address. Redistribution subject to ECS terms of use (see **ecsdl.org/site/terms_use**) unless CC License in place (see abstract).